Available online at www.sciencedirect.com
ScienceDirect
International Journal of Heat and Fluid Flow 28 (2007) 418–428
International Journal of HEAT AND FLUID FLOW
www.elsevier.com/locate/ijhff

Computations of a turbulent wake in a strong adverse pressure gradient

M.J. Tummers [a,*], K. Hanjalić [a], D.M. Passchier [b], R.A.W.M. Henkes [c]

[a] Delft University of Technology, Faculty of Applied Sciences, P.O. Box 5046, 2600 GA Delft, The Netherlands
[b] Delft University of Technology, Faculty of Aerospace Engineering, P.O. Box 5058, 2600 GB Delft, The Netherlands
[c] Shell Global Solutions International B.V., P.O. Box 38000, 1030 BN Amsterdam, The Netherlands

Accepted 3 July 2006
Available online 6 September 2006

Abstract

Numerical solutions of the Reynolds-averaged Navier–Stokes equations are presented for the near wake of a flat plate with and without the effects of an adverse pressure gradient. The comparison with experiments indicates that both the standard k–ϵ model and a Reynolds-stress transport model accurately reproduce the centreline velocity and the turbulent kinetic energy in the zero-pressure-gradient near wake. In the adverse-pressure-gradient wake, however, none of the turbulence models tested was able to predict the measured mean-flow reversal near the centreline, and the large rise in turbulence kinetic energy in the wake. Examination of the measured and computed kinetic energy budgets in the wake indicated that this discrepancy is due to an incorrect response of the dissipation equation to a spectral imbalance noticed in the experiments.

Keywords: High-lift aerodynamics; Turbulent wake; Adverse pressure gradient; k–ϵ model; Reynolds-stress transport model

1. Introduction

The wing of a transport aircraft is designed to give optimum performance during cruise flight. Such a wing is usually not well suited to generate sufficient lift at low speed as needed during take off and landing. To generate the required lift at low speed the shape of the wing is adapted in flight by means of a mechanical high-lift system comprising trailing-edge flaps and, often, leading-edge slats. The increased camber and the larger chordwise extent of a multi-element airfoil will increase the lift. However, as discussed by Smith (1975), the main contribution to the lift increase stems from the successful manipulation of the pressure distribution by the "gaps" between the different airfoil elements. Smith's classical paper greatly contributed to the understanding of the physics of the flow around a multi-element airfoil. However, 30 years later the aerodynamic design of a high-lift system still is a challenging problem. Major causes for this are the various phenomena that affect the flow around a multi-element airfoil (see e.g. Butter, 1984 or Meredith, 1992). A number of these phenomena are listed below and illustrated in Fig. 1.

- The large suction peak on the most forward element may cause local supersonic flow, even if the free-stream Mach number is as low as 0.2. The shock wave interacts with the boundary layer on the slat.
- Near the sharp edge of a cavity the boundary layer is forced to separate and a recirculation zone is formed in the cavity.
- Near the leading edge of the main element the turbulent boundary layer may relaminarize as a result of strong favourable pressure gradients.
- At high angles of attack, the slat wake may become confluent with the boundary layer on the main element. The wake of the main element may interact with the boundary layer that develops on the flap.

* Corresponding author. Tel.: +31 152 782477; fax: +31 152 781204.
E-mail address: mark@ws.tn.tudelft.nl (M.J. Tummers).

0142-727X/$ - see front matter © 2006 Elsevier Inc. All rights reserved.
doi:10.1016/j.ijheatfluidflow.2006.07.002

Nomenclature

C_{ϵ_1}	closure coefficient	$\overline{u'v'}$	Reynolds shear stress
C_{ϵ_4}	closure coefficient	$\overline{u'v'}_s$	Reynolds shear stress in streamline coordinates
C_p	static-pressure coefficient	$\overline{u'^2}$	Reynolds normal stress for x-direction
f_4	damping function	$\overline{v'^2}$	Reynolds normal stress for y-direction
H	shape factor ($=\delta^*/\theta$)	x	coordinate along wind tunnel axis
k	turbulence kinetic energy	y	lateral coordinate
P_k	production of turbulence kinetic energy	δ^*	displacement thickness
$\bar{p}_m$	measured static pressure	ϵ	dissipation rate
S_{ϵ_4}	term in transport equation for ϵ	θ	momentum thickness
U_{ref}	free-stream velocity	Ω_k	component of vorticity vector ($=\epsilon_{ijk}\partial\bar{u}_i/\partial x_j$)

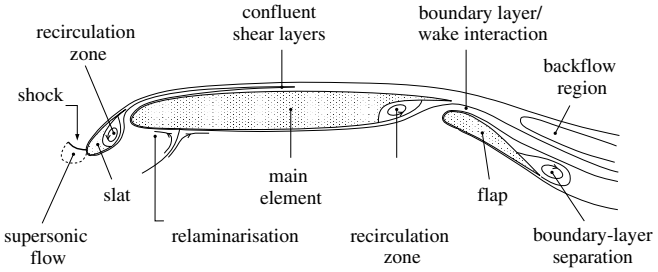

Fig. 1. Phenomena that affect the flow around a multi-element airfoil.

- Due to the large effective camber the shear layers are strongly curved, giving rise to significant static-pressure variations across the shear layers.
- Strong adverse pressure gradients promote the growth of wakes and boundary layers, and can lead to flow separation.

Considering the complexity of the different flow phenomena, and their possible interactions, it is not surprising that the numerical prediction of the flow around a multi-element airfoil is extremely difficult.

Adair and Horne (1989) argued that modern computational methods based on the Reynolds-averaged Navier–Stokes (RANS) equations can accurately predict the lift up to moderate angles of attack, provided the flow remains attached, whereas the drag cannot be predicted accurately. At higher angles of attack, i.e. near the maximum-lift conditions, the computational methods fail to predict correctly either the lift or the drag. More than a decade later the situation was essentially still the same (see e.g. Rumsey and Ling, 2002). The improvement of the existing calculation methods with advanced grid generation and numerical schemes did not help much, thus leaving the turbulence models as the source of uncertainty. Developing turbulence models that properly describe the different phenomena essential to the flow around high-lift systems requires a better understanding of the physics of these flows, which can be achieved by studying various phenomena and specific features in isolation. For example, experimental investigations of elementary flows, such as a turbulent boundary layer that separates from a wall (Simpson et al., 1981; Simpson, 1989), the development of a curved wake (Ramjee et al., 1987) or the flow over a backward-facing step (Eaton and Johnston, 1981), provide insight into the different flow phenomena.

This investigation is related to one particular feature of high-lift aerodynamics, i.e. the wake flow in the trailing-edge region of the main element. This wake is very complex because it is subjected to strong pressure gradients in streamwise and lateral directions. In the present investigation this problem was simplified to the analysis of the wake of a "thick" flat plate with a tapered trailing edge that was subjected to a strong adverse pressure gradient. The accurate prediction of the near wake of a flat plate can be seen as a first step in the development of computational model capable of predicting the wakes of more realistic configurations that include the complicating effects of curvature, asymmetry and large streamwise pressure gradients.

The computational studies by Patel and Scheuerer (1982) and Patel and Chen (1987) have shown that the standard k–ϵ model accurately reproduces the main features of the near wake of a thin flat plate in zero pressure gradient.

The first part of this paper evaluates the performance of the standard k–ϵ model and a Reynolds-stress transport model to predict the near wake of a tapered flat plate in the absence of external pressure gradients. Clearly, a tapered trailing edge is a more realistic simulation of the near wakes of airfoils. The tapering causes a disturbance of the pressure distribution in the trailing-edge region that influences the flow in the near wake. In the second part of the paper, the flow in the trailing-edge region of the same tapered flat plate is subjected to a severe adverse pressure gradient that causes high turbulence intensities and local mean-flow reversal. The region with mean-flow reversal in the wake is not connected to the trailing edge. This flow phenomenon is known as "free separation" or "off-body separation." There are several reports in the literature (e.g. Petrov, 1980) claiming that free separation can occur in the wake of the main element during the final stall.

In a pioneering study of strongly decelerated wakes Hill et al. (1963) succeeded in reproducing the mean-flow reversal reasonably well with a simple calculation method based on von Kármán's integral momentum equation and an eddy viscosity that is uniform across the wake. To achieve agreement between the measured and computed mean-velocity profiles, Hill et al. made ad hoc changes to a coefficient in the expression for the eddy viscosity, but they could not indicate whether the turbulence was predicted accurately, because the measurements were limited to time-averaged values of velocity and pressure. In retrospect, this apparent ease to reproduce the mean flow in strongly decelerating wakes has fed the belief that strong streamwise pressure gradients do not pose serious problems when predicting near wakes of streamlined bodies. During the nineties it became clear that this was incorrect. The investigations by Tummers et al. (1997), Hoffenberg and Sullivan (1998) and Driver and Mateer (2002) have indicated that standard two-equation models and Reynolds-stress transport models have difficulties in accurately predicting the mean-flow field and the turbulence of the adverse-pressure-gradient wake in case free separation occurs. However, from these investigations it is not clear what the origin of these difficulties is. It is the objective of this work to shed some light on this issue.

2. Flow configuration

The experimental set-up used to investigate the adverse-pressure-gradient wake is described in detail in a previous paper (Tummers et al., 2006). Therefore, only the main features of the set-up are given here. A flat plate was used as a wake generator. The plate was mounted at zero angle of attack in the test section (400×400 mm^2) of an open-return wind tunnel as shown in Fig. 2. The plate has a 600-mm chord and a thickness of 18 mm. The last 110 mm were tapered to form a sharp trailing edge. The boundary layers on both sides of the plate were tripped with wires positioned at 6% chord to ensure uniform laminar-turbulent transition across the span.

To subject the wake to an adverse pressure gradient, the test section was followed by a two-dimensional diffuser whose side walls are positioned at a 15° divergence angle. The walls of the diffuser were fitted with a large number of regularly spaced suction slots to prevent boundary-layer separation on the diffuser walls. For the zero-pressure-gradient case, the diffuser formed a straight channel with a nearly constant cross section.

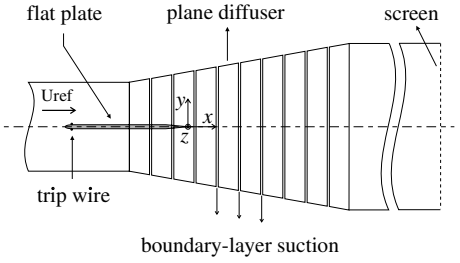

Fig. 2. Test configuration for the investigation of the wake in adverse pressure gradient.

The wind tunnel was operated at a fixed chord-Reynolds number of 4×10^5, corresponding to a free-stream velocity, U_{ref}, of about 10.2 m/s. This velocity was used to non-dimensionalize all measured data. The data are presented in an orthogonal coordinate system. The x-coordinate, with origin at the plate's trailing edge at half span, is directed downstream along the tunnel axis. The y-coordinate is measured normal to the symmetry plane (see Fig. 2).

3. Numerical investigation

The Reynolds-averaged continuity and momentum equations were numerically solved for the two-dimensional, turbulent near wake both for the constant pressure and the adverse-pressure-gradient cases. Two turbulence models were considered; the two-equation k–ϵ model of Launder and Sharma (1974) and the Reynolds-stress transport model of Hanjalić et al. (1999). Details on both turbulence models are given in Appendix A.

3.1. Numerical procedure and boundary conditions

To solve the equations numerically, the spatial derivatives in the equations are discretized with the finite volume method on a staggered grid. A Cartesian grid was used with a refinement in the y-direction near the centreline, whereas the grid was equidistant in the x-direction. The convection terms are discretized with the second-order accurate upwind scheme. An unsteady fully implicit time integration is performed to obtain the steady solution at large time. At each new time level the discrete systems belonging to each of the transport equations are iteratively solved by a line Gauss–Seidel method. Alternating Gauss–Seidel sweeps from the west to the east side and from the east to the west side of the computational domain are performed. After each sweep the pressure is calculated from the discretized Poisson equation for the pressure correction by using a conjugate gradient solver. The calculation was started with a certain initial solution at $t = 0$ and the time integration is performed until a steady final solution is reached. A time-resolved solution was not obtained since the (false) time steps were taken relatively large.

The boundary conditions for the computations in the wake were specified as follows. The inlet (west) was taken at $x = 17$ mm for the adverse-pressure-gradient case, and at $x = 2.5$ mm for the zero-pressure-gradient wake. At the inlet the measured mean-velocity profiles and the turbulence profiles are prescribed, whereas the inlet profile for ϵ is guessed by assuming a local equilibrium of production and dissipation of turbulent kinetic energy, i.e. $\epsilon = P_k$. The consequences of this somewhat inaccurate assumption regarding the ϵ inlet profile will be discussed later.

At the outer edge of the wake (located at $y = 200$ mm for the adverse-pressure-gradient case and at $y = 80$ mm for the zero-pressure-gradient case) the measured static pressure is prescribed. Homogeneous Neumann conditions are prescribed for all turbulence quantities. Varying the position of the wake outer edge was verified to have negligible effect on the solution. Symmetry was assumed at the wake centreline ($y = 0$ mm). Therefore, only one half of the wake was calculated. Zero streamwise gradients were assumed at the end of the computational domain ($x = 600$ mm). Tests were carried out in which the downstream end of the domain was varied between $x = 600$ mm and $x = 1200$ mm. There was no significant effect of this variation in the region where experimental data were available. Results were obtained on a coarse grid consisting of 50×50 points and on a fine grid with 100×100 points. The differences in the results on these two grids are negligibly small, indicating that almost grid-independent solutions were obtained.

4. Results for the zero-pressure-gradient wake

The studies by Patel and Scheuerer (1982) and Patel and Chen (1987) have shown that a standard k–ϵ model accurately reproduced the main features of the near wake of a *thin* flat plate in zero pressure gradient. However, in the present study a *thick* plate with a tapered trailing edge is used. The pressure variations induced by the taper may have significant effects on the flow in the trailing-edge region. Therefore, one cannot exclude beforehand the possibility that the "internal" pressure variation caused by the tapering poses a problem to the turbulence models that prevents successful prediction of this near wake. It will be shown here that this is not the case.

The measured and the computed centreline velocity for the wake in zero pressure gradient (zpg) are shown in Fig. 7 (left). The turbulent kinetic energy on the centreline and the maximum value of the turbulent kinetic energy at various x-stations are shown in Fig. 3. Both graphs indicate good agreement between the experiments and the numerical predictions. The streamwise development of the displacement thickness, δ^*, and the momentum thickness, θ, are given in Fig. 4. The upper and the lower limits in the integrals defining δ^* and θ for the computed mean-velocity profiles was chosen as the largest and the smallest y-coordinate of the measurement grid at each x-station. The computations accurately reproduce the measured decrease of the momentum thickness from $\theta = 4.7$ mm at the trailing edge to $\theta = 3.3$ mm further downstream.

The variation of the momentum thickness in the zero-pressure-gradient wake can be explained from the computed static-pressure distribution in the near wake. The static pressure is practically constant at the outer edge of the computational domain at $y = 80$ mm. (This boundary condition followed from the static-pressure measurements.) The static pressure is also practically constant far downstream of the trailing edge. There, the very small static-pressure variations in y-direction are caused by the variation of

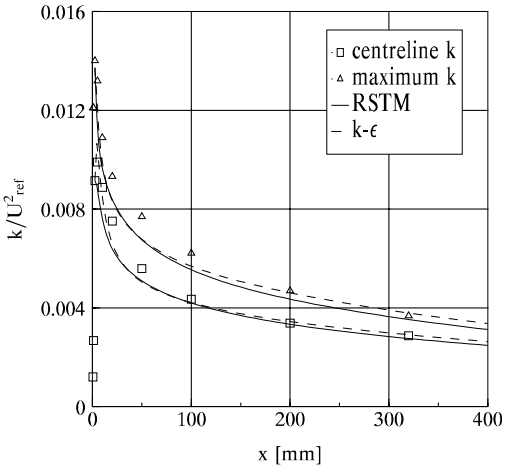

Fig. 3. The turbulent kinetic energy for the wake in zero pressure gradient.

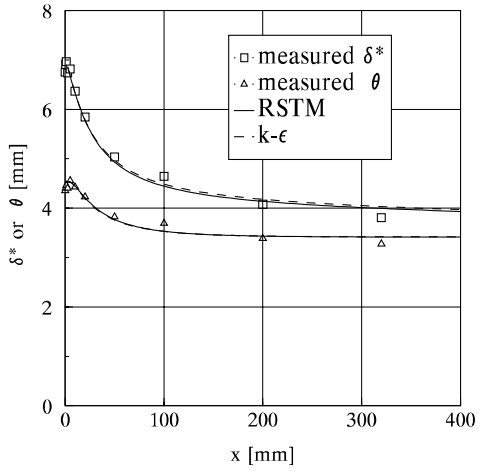

Fig. 4. The displacement thickness δ^* and the momentum thickness θ for the wake in zero pressure gradient.

the Reynolds stress $\overline{v'^2}$ with y, in agreement with the Reynolds-averaged momentum equation for the y-direction. However, there are significant pressure gradients in both lateral and streamwise direction near the trailing edge of the plate. These "internal" pressure variations are a result of the tapering of the trailing edge. The taper causes an increase of the static pressure in the boundary layer when moving towards the trailing edge. This explains the relatively high value of the shape factor ($H \equiv \delta^*/\theta = 1.55$) of the mean-velocity profile at $x = 0$ mm. The pressure decreases directly downstream of the trailing edge such that the near wake experiences a favourable pressure gradient thus giving rise to a decrease of the momentum thickness.

5. Results for the adverse-pressure-gradient wake

5.1. Mean velocity and kinetic energy

Figs. 5 and 6 show the measured and calculated x-component of the mean velocity $\bar{u}$ and the kinetic energy k at

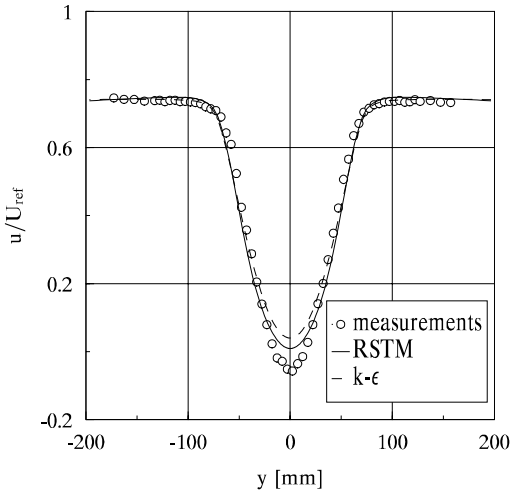

Fig. 5. Measured and calculated mean velocity at $x = 175$ mm for the adverse-pressure-gradient wake.

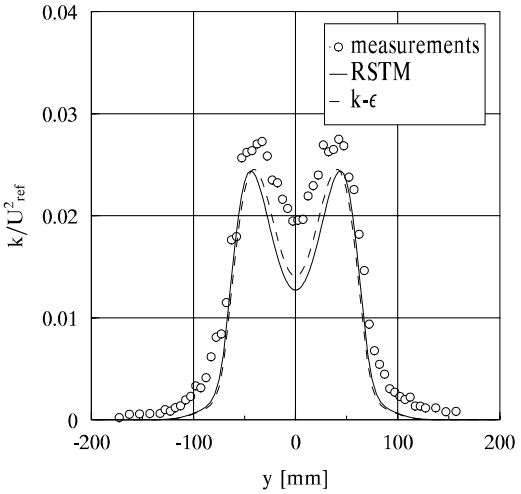

Fig. 6. Measured and calculated kinetic energy at $x = 175$ mm for the adverse-pressure-gradient wake.

station $x = 175$ mm. An important observation is that the width of the wake, and thus the spreading rate, appears to be well predicted. However, at the edge of the wake the measured kinetic energy is higher than the computed values. This may be caused by the intermittent behaviour of the interface that separates turbulent from non-turbulent air. An explicit modeling of the effects of the intermittency, as suggested by e.g. Cho and Chung (1992), may reduce the discrepancies between the measurements and the computations near the edge of the wake. However, the effects of such a modification of the turbulence models were not explored in the present investigation. There are larger discrepancies between the experiments and the predictions near the centreline of the wake. This is further illustrated in Fig. 7 which shows the mean velocity and the kinetic energy along the centreline. For a fair comparison, the results for the zero-pressure-gradient wake are also included. The graph shows that neither model is able to reproduce the measured mean-flow reversal for the adverse-pressure-gradient flow. The RSTM is only slightly more accurate than the k–ϵ model as far as the mean velocity is concerned. One may argue that the differences between measured and computed centreline velocities are (although larger than those for the constant pressure gradient case) only 10% of the velocity defect. At first sight this 10% difference may not seem very important. However, in the stall mechanism of a multi-element airfoil described by, e.g., Johnston and Horton (1986) and Petrov (1980), the abrupt loss of lift is precipitated by the mean-flow reversal in the adverse-pressure-gradient wakes developing above the main element. Therefore, not reproducing mean-flow reversal does have serious consequences for the ability of computational codes to predict the final stall of a multi-element airfoil.

It may be argued that the size and position of regions of reversed flow are often sensitive to the strength of the pressure gradient, so that a slight inaccuracy in the prescribed static-pressure distribution at the outer edge of the wake ($y = 200$ mm) may alter the mean flow significantly. For the present flow this sensitivity was investigated by means of a comparison of the numerical solutions for slightly different pressure gradients. The results of the analysis are given in Fig. 8. The curve for $\bar{p} = \bar{p}_m$ is the numerical solution of the RSTM for the measured static-pressure distribution. Of course, the curves for $\bar{p} = \bar{p}_m$ are identical to those shown in Fig. 7. The other two curves are the results for $\bar{p} = c\bar{p}_m$, where c was varied between 0.95 and 1.05 to simulate an error in the measured static-pressure distribution. It is seen that a 5% error in the static pressure has only a small effect on the mean velocity on the wake centreline. The difference between the measured and the calculated mean velocity on the centreline is much larger and cannot be explained from a possible error in the measured static-pressure distribution. Fig. 8 also indicates that a 5% error in the static pressure has negligible effect on the kinetic-energy level on the centreline.

Another point of concern is the effect of an inaccurate inflow condition for the dissipation. The results presented so far pertain to the initial condition $\epsilon = P_k$. However, the measured balance of the kinetic-energy equation shown in Fig. 12, indicates that the assumption $\epsilon = P_k$ is inaccurate. It seems therefore more realistic to use the dissipation profile that was determined from the balance of the kinetic-energy equation at $x = 30$ mm, denoted by $\epsilon = \epsilon_{\text{balance}}$, as an inflow condition for the dissipation. The results of the RSTM for this new boundary condition are shown in Fig. 8 (dashed lines). It is seen that the new boundary condition for ϵ has resulted in a generally higher kinetic-energy level, although the computed level is still much lower than the measured values of k at large trailing-edge distances. Also, the mean velocity on the centreline has slightly increased. So, despite the more realistic inflow condition for the dissipation, there is no overall improvement of the numerical prediction. The same conclusion was drawn from the predictions of the k–ϵ

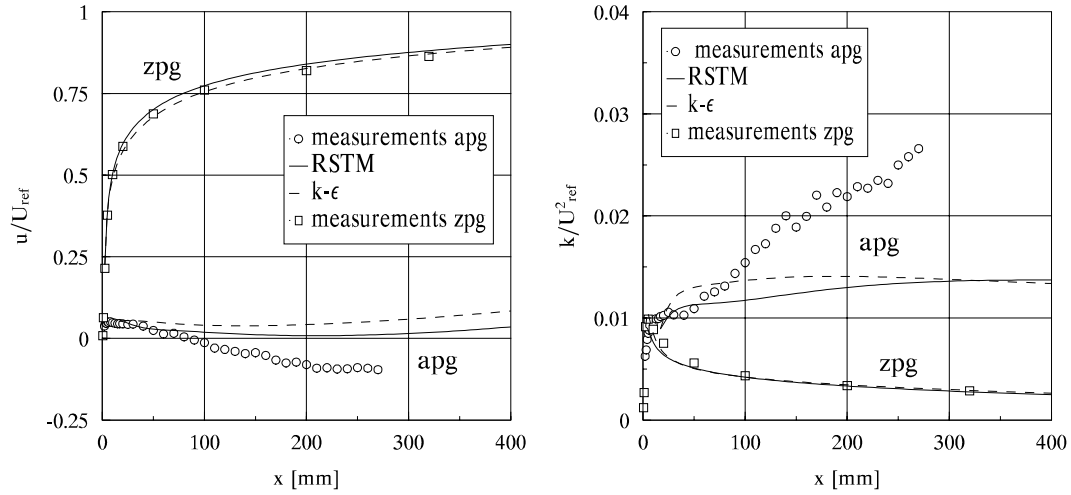

Fig. 7. Measured and calculated mean velocity (left) and kinetic energy (right) along the centreline.

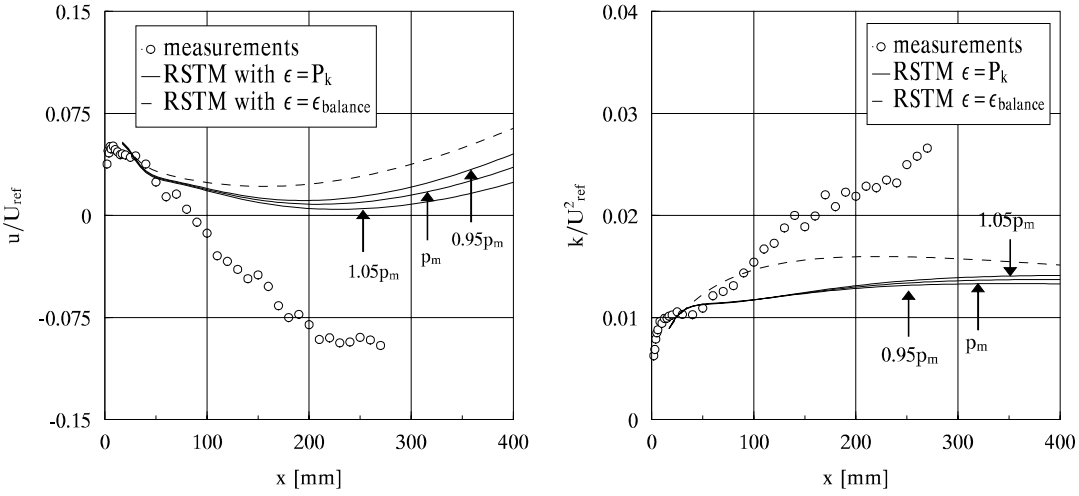

Fig. 8. The effect of static-pressure variations and the initial ϵ profile on the outcome of the RSTM.

model with $\epsilon = \epsilon_{\text{balance}}$ as a boundary condition. These results are not shown here for brevity.

5.2. Prediction of the Reynolds-stress anisotropy

It is seen in Fig. 7 that the kinetic energy on the centreline is strongly underpredicted. However, the distribution of the kinetic energy over the different Reynolds normal stresses, as found with the RSTM, agrees quite well with the experiments. This can be observed in Fig. 9 which shows the measured and the computed values of $\gamma_\alpha = \overline{u_\alpha'^2}/(2k)$ on the wake centreline. These results confirm that the model for the pressure strain in the RSTM is satisfactory, but also indicate a deficiency in the ϵ-equation.

5.3. Predictions of Reynolds shear stress and kinetic energy

Fig. 10 compares the measured and the calculated Reynolds shear stress, $-\overline{u'v'}_s$, for the k–ϵ model and the RSTM.

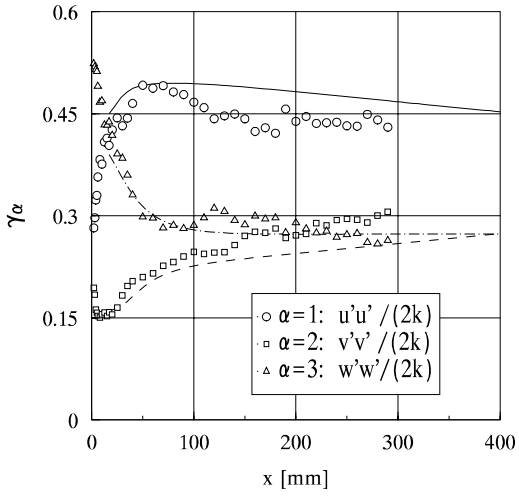

Fig. 9. Measured and computed values of the anisotropy parameter γ_α on the centreline. The symbols represent the measurements; the lines are the results for the RSTM.

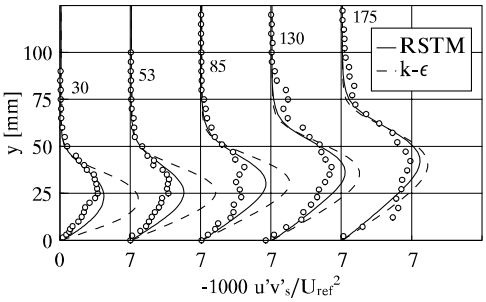

Fig. 10. Measured and computed Reynolds-shear-stress profiles for the k–ϵ model (dashed lines) and the RSTM (full lines).

The k–ϵ model overpredicts the shear-stress values everywhere. This is attributed to the insensitivity of the k–ϵ model (especially the ϵ-equation) to strong adverse pressure gradients leading to separation, as well as the insensitivity of eddy-viscosity models in general to the specific stress anisotropy generated by the adverse pressure gradient. To this one can add a strong flow inhomogeneity close to the wall which, apart from equilibrium flows where the models is tuned, cannot be well reproduced by any eddy-viscosity model.

It is seen in Fig. 10 that the RSTM yields better predictions of the Reynolds-shear-stress profiles than the k–ϵ model. However, the RSTM also tends to overpredict the Reynolds shear stress. The predicted gradients of $-\overline{u'v'}_s$ in y-direction on the centreline are larger than the measured gradients, especially for the upstream stations. This is a serious shortcoming, because too high Reynolds-shear-stress gradients result in a too fast increase of the mean velocity on the centreline. The consequences of this can be observed in Fig. 7.

Even though the RSTM gives much better predictions of the Reynolds shear stress than the k–ϵ model, there is not much difference between the two models as far as the kinetic energy is concerned. As seen in Fig. 11, the RSTM is slightly more accurate for the measuring stations close to the trailing edge, but both models tend to underpredict the kinetic-energy levels farther in the wake.

The reader may wonder why the much better shear stress predictions for the RSTM (as compared to those for the k–ϵ model) have resulted in only a marginal improvement of the centreline velocity predictions. To understand this, attention should be directed to the Reynolds normal stresses. The analysis of the different terms in the Reynolds-averaged momentum equation (see Fig. 18 in Tummers et al., 2006) has indicated that the Reynolds shear stresses and the Reynolds normal stresses are of equal importance in this adverse-pressure-gradient wake. Therefore, accurate predictions of the Reynolds shear stresses do not guarantee correct mean-flow behaviour unless the Reynolds normal stresses are also predicted accurately. Fig. 7 (right) indicates that both models strongly underpredict the Reynolds normal stresses along the centreline. The underestimation of the Reynolds normal stress gradient $\partial\overline{u'^2}/\partial x$ contributes to the too high mean velocity on the centreline.

5.4. The computed kinetic-energy balances

Fig. 12 shows the measured and computed balances of the kinetic-energy equation at station $x = 30$ mm for the k–ϵ model and the RSTM. Both the dissipation and the production of kinetic energy are strongly overestimated by the k–ϵ model, but the predictions of the RSTM agree well with the experimental results. The ratio of production and dissipation P_k/ϵ, determined at the location of maximum production, is 1.61 for the k–ϵ model and 1.27 for the RSTM. The measurements indicate $P_k/\epsilon = 1.3$.

The RSTM produces better results for the transport terms than the k–ϵ model. However, neither the k–ϵ model nor the RSTM reproduces the significant advection of k near the edge of the wake caused by the transport by turbulent velocity fluctuations. As a result, both turbulence models fail to predict the relatively high kinetic-energy levels near the edge of the wake as observed in Fig. 6.

Fig. 13 shows the measured and computed kinetic-energy balances as determined at $x = 130$ mm for the k–ϵ model and the RSTM. Several interesting observations can be made. For example, both models computed almost the same values of the production of turbulence kinetic

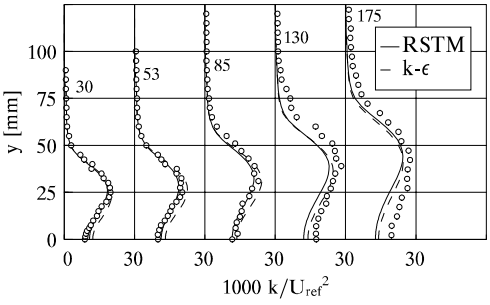

Fig. 11. Measured and computed kinetic-energy profiles for the k–ϵ model (dashed lines) and the RSTM (full lines).

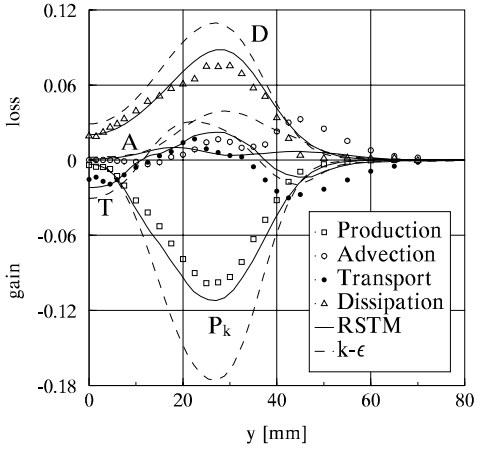

Fig. 12. Measured and computed kinetic energy balance at station $x = 30$ mm. The dashed lines are the results for the k–ϵ model.

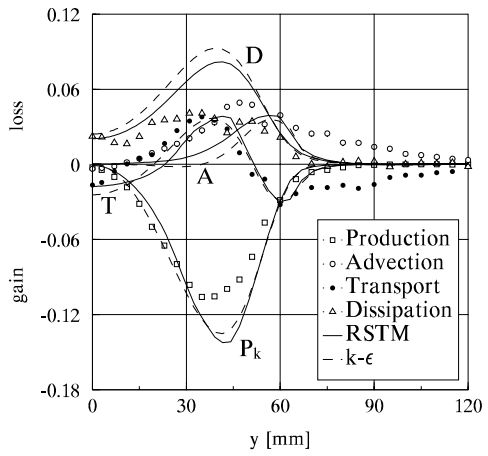

Fig. 13. Measured and computed kinetic energy balance at station $x = 130$ mm. The dashed lines are the results for the k–ϵ model.

energy P_k (and these values are only slightly larger than the measured values). However, the most important observation is that both models predicted a much too high dissipation level. Neither model has predicted the large decrease of the measured dissipation in between $x = 30$ mm and $x = 130$ mm. Instead, both models predicted relatively small changes of the dissipation levels in the streamwise direction. It can therefore be concluded that, even though the computed production of kinetic energy P_k is nowhere smaller than the measured P_k, the computations yield too low levels of k, because the computed dissipation of turbulence kinetic energy is too high.

The fact that *both* models computed too high dissipation levels at the more downstream station is indicative of a deficiency in the transport equation for the dissipation ϵ. The transport equation for the dissipation in the k–ϵ model (Eq. (5) in Appendix A) and the transport equation for the homogeneous part of the dissipation in the RSTM (Eq. (20) in Appendix A) are very similar. In particular, in both equations the production of ϵ is directly linked to the production of turbulence kinetic energy P_k. If this model for the production of ϵ is inaccurate in the present wake flow, then the superiority of the RSTM over the standard k–ϵ model is negated by the use of an improper scale-providing ϵ-equation, despite the apparently good model of the pressure redistribution.

The spectral density functions (sdfs) that were measured in the adverse-pressure-gradient wake (reported in detail in Tummers et al., 2006) explain the failure of the model for the source term in the transport equation for the dissipation. The measured sdfs clearly indicate the presence of turbulence structures that are characterised by very low frequencies. Such turbulence structures are absent in the trailing-edge region of the flat plate in case of a zero pressure gradient. Because the near wake of the flat plate in zero pressure gradient can be accurately predicted by the standard k–ϵ model and the RSTM, it is plausible to assume that the failure of the same models to accurately predict the present wake is caused by the low-frequency turbulence structures (which are thought to be roll cells).

In the present adverse-pressure-gradient wake a significant amount of the produced turbulence kinetic energy ends up as low-frequency velocity fluctuations. Unaware of this phenomenon, the transport equation for ϵ in both turbulence models interprets all of the kinetic energy that is produced as conventional "equilibrium turbulence" and produces ϵ at a rate proportional to P_k through the source term: $C_{\epsilon_1} P_k \epsilon / k$. It appears that this is an inaccurate model in the present flow, because the energy transfer to the high-frequency, dissipation range of the spectrum takes place at a rate that is lower than $C_{\epsilon_1} P_k \epsilon / k$ due to the accumulation of the produced turbulence kinetic energy in the low-frequency part of the spectrum.

A possible remedy would be to include the term $S_{\epsilon_4} = -C_{\epsilon_4} f_4 k \Omega_k \Omega_k$ in the transport equation for ϵ (Eq. (20) in Appendix A). The inclusion of S_{ϵ_4} is meant to differentiate the effects of the "rotational strains" and the "irrotational strains" on the source dissipation, as suggested by Hanjalić and Launder (1980). In case the mean flow is two-dimensional this term reduces to

$$S_{\epsilon_4} = C^*_{\epsilon_4} \frac{\epsilon}{k} \left(\overline{v'^2} - \overline{u'^2} \right) \frac{\partial \bar{u}}{\partial x},$$

where $C^*_{\epsilon_4}$ is a closure coefficient with standard value 1.16. It was shown in Jakirlić et al. (1994) and Henkes (1997) that the inclusion of the term S_{ϵ_4} works very well in boundary layers subjected to adverse pressure gradients.

In the adverse-pressure-gradient wake with $\partial \bar{u} / \partial x < 0$ and $\overline{v'^2} < \overline{u'^2}$, the additional term S_{ϵ_4} will be positive for positive values of $C^*_{\epsilon_4}$, thereby increasing the dissipation while reducing the kinetic energy. The smaller kinetic energy together with the larger dissipation reduces the eddy viscosity, which in turn reduces the mean velocity on the centreline. The inclusion of S_{ϵ_4} (with $C^*_{\epsilon_4} > 0$) indeed improved the agreement between measurements and computations as far as the mean velocity is concerned. However, the price paid for this improvement is a worsening of the numerical predictions of the kinetic energy. For the standard value of $C^*_{\epsilon_4} = 1.16$, the extra term in the dissipation equation caused a dramatic decrease of k along the centreline, so that the flow nearly relaminarized. Such a behaviour is not in accordance with the experiments.

To improve the performance of two-equation models in adverse-pressure-gradient flows, Menter (1994) suggested to use a modified eddy viscosity as in

$$\nu_t = \frac{ak}{\max\{a\omega; S\}}, \tag{1}$$

where $\omega \equiv \epsilon / k$ is the dissipation per unit turbulence kinetic energy, S is the mean strain-rate tensor, and $a \equiv -\overline{u'v'}/k$ is a "structural parameter" which is supposed to be constant and approximately equal to 0.3. In an adverse-pressure-gradient flow, the production of k is larger than the dissipation, so that the above expression for the eddy viscosity reduces to $\nu_t = ak/S$. However, this modified eddy viscosity

was not tested here, since it was known from the experiment that the structural parameter a was not constant in the present adverse-pressure-gradient flow as can be seen from Fig. 15 in Tummers et al. (2006).

6. Conclusion

Numerical solutions of the RANS equations were obtained for the near wake of a tapered flat plate with and without an externally imposed pressure gradient. The predictions of the standard k–ϵ model and a Reynolds-stress transport model (RSTM) were in good agreement with the experiments for the zero-pressure-gradient wake. The agreement between the experiments and the predictions for the adverse-pressure-gradient wake was less satisfactory. Neither model reproduced the experimentally found mean-flow reversal together with the large increase of the turbulent kinetic energy on the wake centreline. Whenever major differences occurred between the predictions of the k–ϵ model and the RSTM, the latter proved to be superior. For example, the RSTM predicted more accurate Reynolds shear stresses than the k–ϵ model. The RSTM was also able to predict the anisotropy of the Reynolds normal stresses with good accuracy. However, the overall performance of the RSTM is not better than that of the standard k–ϵ model for the present adverse-pressure-gradient wake flow.

A comparison between the measured and the computed kinetic-energy balances indicated that both models predicted too high dissipation levels, indicating a deficiency in the transport equation for the dissipation ϵ, which are rather similar in both models. Spectral density functions measured in the adverse-pressure-gradient wake revealed an anomaly where a significant amount of kinetic energy accumulates in the very low-frequency range, possibly due to the formation of roll cells. However, the transport equation for ϵ in both turbulence models is unaware of this phenomenon, and interprets all of the produced kinetic energy as conventional equilibrium turbulence, thereby producing too high dissipation levels.

Appendix A

A.1. Low-Reynolds-number k–ϵ model

The k–ϵ model employs the Boussinesq approximation, which relates the Reynolds stresses to the mean strain rate according to

$$-\overline{u_i'u_j'} = \nu_t\left(\frac{\partial \overline{u_i}}{\partial x_j}+\frac{\partial \overline{u_j}}{\partial x_i}\right)-\frac{2}{3}k\delta_{ij}, \tag{2}$$

where ν_t is the eddy viscosity:

$$\nu_t = c_\mu f_\mu \frac{k^2}{\epsilon}. \tag{3}$$

The kinetic energy k and the turbulent energy dissipation ϵ are described by the following two differential equations:

$$\frac{\partial k}{\partial t}+\overline{u_j}\frac{\partial k}{\partial x_j} = \frac{\partial}{\partial x_j}\left[\left(\nu+\frac{\nu_t}{\sigma_k}\right)\frac{\partial k}{\partial x_j}\right]-\epsilon+D + \nu_t\left(\frac{\partial \overline{u_i}}{\partial x_j}+\frac{\partial \overline{u_j}}{\partial x_i}\right)\frac{\partial \overline{u_i}}{\partial x_j} \tag{4}$$

and

$$\frac{\partial \epsilon}{\partial t}+\overline{u_j}\frac{\partial \epsilon}{\partial x_j} = \frac{\partial}{\partial x_j}\left[\left(\nu+\frac{\nu_t}{\sigma_\epsilon}\right)\frac{\partial \epsilon}{\partial x_j}\right]+E+c_{\epsilon_1}f_1\frac{\epsilon}{k}P_k-c_{\epsilon_2}f_2\frac{\epsilon^2}{k}. \tag{5}$$

The low-Reynolds-number functions f_μ, f_1, f_2, D and E bring into account the effects of wall proximity and viscosity. An overview of different low-Reynolds-number formulations is given by Patel et al. (1985). In the present investigation the formulation of Launder and Sharma (1974) is adopted, i.e.

$$\begin{aligned} f_\mu &= \exp\left(\frac{-3.4}{(1+Re_t/50)^2}\right),\\ f_1 &= 1.0,\\ f_2 &= 1.0-0.3\exp(-Re_t^2),\\ D &= -2\nu\frac{\partial\sqrt{k}}{\partial x_j}\frac{\partial\sqrt{k}}{\partial x_j},\\ E &= 2\nu\nu_t\frac{\partial^2\overline{u_i}}{\partial x_j\partial x_k}\frac{\partial^2\overline{u_i}}{\partial x_j\partial x_k}, \end{aligned} \tag{6}$$

where Re_t is the turbulent Reynolds number, defined as

$$Re_t = \frac{k^2}{\nu\epsilon}. \tag{7}$$

The high-Reynolds-number closure coefficients have the standard values (Launder and Sharma, 1974): $c_\mu = 0.09$, $c_{\epsilon_1} = 1.44$, $c_{\epsilon_2} = 1.92$, $\sigma_k = 1.0$ and $\sigma_\epsilon = 1.3$.

A.2. Reynolds-stress transport model

The Reynolds-stress transport model (RSTM) has its origin in the exact transport equation for the Reynolds stresses:

$$\frac{\partial \overline{u_i'u_j'}}{\partial t}+\overline{u_k}\frac{\partial \overline{u_i'u_j'}}{\partial x_k} = -\left(\overline{u_i'u_k'}\frac{\partial \overline{u_j}}{\partial x_k}+\overline{u_j'u_k'}\frac{\partial \overline{u_i}}{\partial x_k}\right)+\frac{\partial}{\partial x_k}\nu\frac{\partial \overline{u_i'u_j'}}{\partial x_k} + D_{ij}^t+\Phi_{ij}-\epsilon_{ij}. \tag{8}$$

The generalized gradient-diffusion hypothesis (Daly and Harlow, 1970) is used for D_{ij}^t, i.e.

$$D_{ij}^t = \frac{\partial}{\partial x_k}\left[C_s\frac{k}{\epsilon}\overline{u_k'u_l'}\frac{\partial \overline{u_i'u_j'}}{\partial x_l}\right], \tag{9}$$

where C_s is a closure coefficient with value 0.22. The pressure-strain correlation, Φ_{ij}, is split into two parts,

$$\Phi_{ij} = \Phi_{ij,1} + \Phi_{ij,2}. \tag{10}$$

The slow pressure strain, $\Phi_{ij,1}$, is modeled using Rotta's "return-to-isotropy hypothesis," i.e.

$$\Phi_{ij,1} = -C_1 \epsilon a_{ij}, \tag{11}$$

where a_{ij} is the Reynolds-stress anisotropy tensor, defined as

$$a_{ij} = \frac{\overline{u_i' u_j'}}{k} - \frac{2}{3}\delta_{ij}. \tag{12}$$

The rapid-strain term, $\Phi_{ij,2}$, is modeled using the "isotropization-of-production hypothesis" (Launder et al., 1975)

$$\Phi_{ij,2} = -C_2\left(P_{ij} - \frac{2}{3}P_k\delta_{ij}\right), \tag{13}$$

where $P_k = \frac{1}{2}P_{ii}$ is the production of the turbulence kinetic energy, k. The C_1 and C_2 that appear in Eqs. (11) and (13), respectively, are functions of the turbulent Reynolds number, Re_t, and parameters derived from the Reynolds-stress anisotropy tensor, such as the "flatness," A, defined by

$$A = 1 - \frac{9}{8}(A_2 - A_3), \tag{14}$$

where $A_2 = a_{ij}a_{ji}$ and $A_3 = a_{ij}a_{jk}a_{ki}$ are the first and second invariants of the Reynolds-stress anisotropy tensor, a_{ij}. The values of C_1 and C_2 depend on Re_t, A_2 and A_3 as suggested by Launder and Shima (1989), i.e.

$$C_2 = 0.75A^{1/2}, \tag{15}$$

$$C_1 = 1 - f_s + 2.58AA_2^{1/4}[1 - \exp(-(0.0067Re_t)^2)], \tag{16}$$

where f_s is a low-Reynolds-number function given by

$$f_s = \frac{1}{(1 + 0.1Re_t)}. \tag{17}$$

The dissipation tensor ϵ_{ij} is modeled as

$$\epsilon_{ij} = f_s\epsilon_{ij}^* + (1 - f_s)\frac{2}{3}\delta_{ij}\epsilon, \tag{18}$$

where

$$\epsilon_{ij}^* = \frac{\epsilon}{k}\left[\frac{\overline{u_i'u_j'} + f_s(\overline{u_i'u_k'}n_jn_k + \overline{u_j'u_k'}n_in_k + \overline{u_k'u_l'}n_kn_in_j)}{1 + \frac{3}{2}\frac{\overline{u_p'u_q'}}{k}n_pn_qf_s}\right]. \tag{19}$$

Here, $\vec{n}$ is the unit-vector normal to the wake centreline, i.e. $n_2 = 1$, $n_1 = n_3 = 0$.

The RSTM employs the following differential equation for the homogeneous dissipation ϵ

$$\begin{aligned}\frac{\partial\epsilon}{\partial t} + \overline{u_k}\frac{\partial\epsilon}{\partial x_k} = {} & \frac{\partial}{\partial x_k}\left[\left(\nu + C_\epsilon\frac{k}{\epsilon}\overline{u_l'u_j'}\right)\frac{\partial\epsilon}{\partial x_l}\right] \\ & - C_{\epsilon_1}f_{\epsilon_1}\frac{\epsilon}{k}\overline{u_i'u_j'}\frac{\partial\overline{u_i}}{\partial x_j} - C_{\epsilon_2}f_{\epsilon_2}\frac{\epsilon\tilde{\epsilon}}{k} \\ & + C_{\epsilon_3}\nu\frac{k}{\epsilon}\overline{u_j'u_k'}\frac{\partial^2\overline{u_i}}{\partial x_j\partial x_l}\frac{\partial^2\overline{u_i}}{\partial x_k\partial x_l},\end{aligned} \tag{20}$$

where $\tilde{\epsilon}$ is given by

$$\tilde{\epsilon} = \epsilon - 2\nu\left(\frac{\partial\sqrt{k}}{\partial x_j}\right)^2, \tag{21}$$

so that $\epsilon = 0$ is prescribed at a solid wall. The high-Reynolds-number closure coefficients in Eq. (20) have the following values (Hanjalić et al., 1999)

$$C_\epsilon = 0.18, \quad C_{\epsilon_1} = 1.44, \quad C_{\epsilon_2} = 1.92 \quad \text{and} \quad C_{\epsilon_3} = 0.5.$$

The low-Reynolds-number functions are given by

$$f_{\epsilon_1} = 1.0 \quad \text{and} \quad f_{\epsilon_2} = 1.0 - \frac{0.52}{1.92}\exp(-(Re_t/6)^2).$$

References

Adair, D., Horne, W., 1989. Turbulent separated flow over and downstream of a two-element airfoil. Exp. Fluids (7), 531–541.

Butter, D., 1984. Recent progress on development and understanding of high-lift systems. In: Improvement of Aerodynamic Performance Through Boundary Layer Control and High Lift Systems. pp. 1.1–26.

Cho, J., Chung, M., 1992. A k–ϵ–γ equation turbulence model. J. Fluid Mech. 237, 301–322.

Daly, B., Harlow, F., 1970. Transport equations of turbulence. Phys. Fluids 13, 2634–2649.

Driver, D., Mateer, G., 2002. Wake flow in adverse pressure gradient. Int. J. Heat Fluid Flow 23, 564–571.

Eaton, J., Johnston, J., 1981. A review of research on subsonic turbulent flow reattachment. AIAA J. 19 (9), 1093–1100.

Hanjalić, K., Launder, B., 1980. Sensitizing the dissipation equation to irrotational strains. ASME, J. Fluids Eng. 102, 34–40.

Hanjalić, K., Hadžić, I., Jakirlić, S., 1999. Modeling turbulent wall flows subjected to strong pressure variations. J. Fluids Eng. 121, 57–64.

Henkes, R., 1997. Comparison of turbulence models for attached boundary layers relevant to aeronautics. Appl. Sci. Res. 57 (1), 43–65.

Hill, P., Schaub, U., Senoo, Y., 1963. Turbulent wakes in pressure gradients. J. Appl. Mech. 30 (12), 518–524.

Hoffenberg, R., Sullivan, J., 1998. Measurement and simulation of a decelerated wake. In: AIAA-98 paper 0522.

Jakirlić, S., Hadžić, I., Hanjalić, K., 1994. Computation of non-equilibrium and separating flows at transitional and high re-numbers with a new low re-number second-moment closure model. In: Proceedings of Strömungen mit Ablösung. AGSTAB, DGLR Congress, Erlangen, Germany.

Johnston, L., Horton, H., 1986. An experimental study of turbulent wake/boundary layer mixing flows. In: Proceedings of the International Congress of Aeronautical Sciences (ICAS). pp. 360–369.

Launder, B., Reece, G., Rodi, W., 1975. Progress in the development of a Reynolds-stress turbulence closure. J. Fluid Mech. 68, 537–566.

Launder, B., Sharma, B., 1974. Application of the energy dissipation model of turbulence to the calculation of flow near a spinning disc. Lett. Heat Mass Transfer 1, 131–138.

Launder, B., Shima, N., 1989. Second-moment closure for the near-wall sublayer: development and application. AIAA J. 27 (10), 1319–1325.

Menter, F., 1994. Two-equation eddy-viscosity turbulence models for engineering applications. AIAA J. 32 (8), 1598–1605.

Meredith, P., 1992. Viscous phenomena affecting high-lift systems and suggestions for future cfd development. In: High-Lift System Aerodynamics. pp. 19.1–8.

Patel, V., Chen, H., 1987. Turbulent wake of a flat plate. AIAA J. 25 (8), 1078–1085.

Patel, V., Scheuerer, G., 1982. Calculation of two-dimensional near and far wakes. AIAA J. 20 (7), 900–907.

Patel, V., Rodi, W., Scheuerer, G., 1985. Turbulence models for near-wall and low Reynolds number flows: a review. AIAA J. 23 (9), 1308–1319.

Petrov, A., 1980. Some features of flow past slotted wings. Library translation 2050, Royal Aircraft Establishment, (also Uchenye Zapiski, TsAGI, 8,6, 1977, pp. 119–124).

Ramjee, V., Tulapurkara, E., Rajasekar, R., 1987. Development of an airfoil wake in a longitudinally curved stream. AIAA J. 26 (8), 948–953.

Rumsey, C., Ling, S., 2002. Prediction of high lift: review of present cfd capability. Progr. Aerosp. Sci. 18, 145–180.

Simpson, R., 1989. Turbulent boundary-layer separation. Ann. Rev. Fluid Mech. (21), 205–234.

Simpson, R., Chew, Y.-T., Shivaprasad, B., 1981. The structure of a separating turbulent boundary layer. Part1: mean flow and Reynolds stresses. J. Fluid Mech. 113, 23–51, part 1.

Smith, A., 1975. High-lift aerodynamics. Journal of Aircraft 12 (6), 501–530.

Tummers, M., Passchier, D., Henkes, R., 1997. Experimental investigation of an adverse pressure gradient wake and comparison with calculations. Exp. Thermal Fluid Sci. 14, 17–24.

Tummers, M.J., Passchier, D.M., Bakker, P.G., 2006. Experiments on the turbulent wake of a flat plate in a strong adverse pressure gradient to appear in IJHFF.